Journal of Manufacturing Processes 141 (2025) 1463–1474

Contents lists available at ScienceDirect

Journal of Manufacturing Processes

journal homepage: www.elsevier.com/locate/manpro

Research Article

Characterization and prediction of the electromechanical wear of contact tips during wire arc additive manufacturing of 316L stainless steel

Zaky Hussein [a,*], Katherine Fu [a], Kyle Saleeby [b], Christopher Saldaña [a]

[a] George W. Woodruff School Mechanical Engineering, Georgia Institute of Technology, 801 Ferst Drive NW, Atlanta, 30332, GA, USA
[b] Georgia Tech Manufacturing Institute, 813 Ferst Drive NW, Atlanta, 30332, GA, USA

ARTICLE INFO

Keywords:
Wire arc additive manufacturing
DED-arc
Contact tube wear
Contact tip wear
Process monitoring
Machine learning
Ensemble machine learning

ABSTRACT

This study seeks to better understand the degradation of the contact tip with respect to WAAM for a 316L wire electrode as well as explore methods of monitoring the contact tip state from process data. The contact tip, a consumable component, positions the wire and serves as the electrical contact surface between the wire electrode and the welding power supply. The wear of the contact tip was characterized in terms of material loss and material contamination for a set of tips worn to discrete levels as measured by the amount of wire fed or arc time. Geometrical characterization found a 49% increase in the bore exit area at 180 meters of wire fed. Machine learning models were developed to predict the relative bore exit area of the contact tip from arc-based process data and a random forest classifier exhibited favorable performance with a cross-validated f1-score of 0.84. The regression architecture implemented a multi-layer perceptron with the ability to predict the relative exit area with an R^2 score of 0.75. Key features used in the prediction include the standard deviation of the voltage and the time between shorts.

1. Introduction

Wire arc additive manufacturing, also known as DED-arc, produces near-net shape components in a layer-by-layer manner by coupling an arc welder with a motion platform, such as a robotic arm or CNC [1,2]. WAAM is of particular interest to the aerospace, naval, tooling and die, and nuclear industries due to WAAM's capability to produce large-scale components of low to medium complexity combined with high deposition rates, low cost of equipment and feedstock, and familiarity with traditional welding [3–5]. Current adoption of the WAAM process is significantly limited by geometrical inaccuracy and defects (voids, gas porosity, cracks, etc.) from the stochastic nature of the electrical arc, improper weld settings or poor process planning [6]. To address these limitations, a considerable body of literature focuses on detecting, mitigating, or controlling defects to ensure the desired geometrical and metallurgical outcomes [7–12]. Low repeatability and geometric accuracy associated with WAAM necessitates controls as well as defect monitoring to produce quality parts. Surprisingly, the contact tube is often overlooked in process monitoring and control schemes in DED-arc, despite serving a key role in the welding systems as it positions the wire feedstock and delivers the welding current.

Research in consumable wear in additive manufacturing gives insight into potential defect formation mechanism, and reduces cost uncertainty serving to increase industry adoption. In powder bed fusion, abrasive wear in the recoater blade causes powder bed streaking, a common defect, which drastically reduces build quality. Worn areas in the recoater blade lead to locally variation in the topology of the powder bed after the recoating pass [13,14]. Current state of the art in process monitoring implements profilometer scans of the bed in between layers or top down imaging to identify such defects in the powder bed surface [15]. Similarly in powder-blown laser directed energy deposition (powder DED-LB), wear of the nozzle changes the powder-gas dynamics and clogs can form on the powder delivery nozzle with both phenomena negatively affecting the powder catchment efficiency [16,17]. In DED-arc, the analog to the powder delivery nozzle would be the contact tube. The contact tube-electrode wire system is a sliding electrical contact, delivering high current loads in a small area. The contact tube wears over time due to adhesive and abrasive wear as wire is continuously fed through the tube under high current loads during the welding process [18]. Wear of the contact tube leads to wire positioning errors, resistance changes, poor arc characteristics, and eventually critical failure in the welding process.

The contact tip or contact tube applies the welding voltage and conducts the current to the consumable wire electrode. Due to the manufacturing process involved in drawing and winding the wire onto

* Corresponding author.
E-mail address: zhussein3@gatech.edu (Z. Hussein).

https://doi.org/10.1016/j.jmapro.2025.03.034
Received 5 November 2024; Received in revised form 28 February 2025; Accepted 5 March 2025

a spool, the wire has a cast or direction it curves in. The wire will form multiple points of contact with the inner surface of the contact tip because of the wire cast [18,19]. Prior research suggests the last point of contact conducts the majority of current and typically occurs in last $\frac{1}{4}$ of contact tip [20]. As a result, the main wear zone is in the last quarter. This portion of the contact tip conducts the most current and subsequently experiences the most ohmic heating, increasing adhesive and abrasive wear. The wire-contact tip interface meets the criterion for abrasive wear as the hardness of steels and other high strength alloys is greater than one and half times the hardness of copper [18,21,22]. Lopez et al. found contamination of steel in near the exit of the contact tip attributed to spatter, and a reduction in hardness of the copper alloy [21]. Additionally, during the welding process small oxides and intermetallic compounds can form in the contact tip leading to asperities forming between the contact tip and wire electrode. Modern contact tips have hardening elements added such as zinc and zirconium, however, evidence of abrasive wear was found in the work done for this study.

Adhesive wear due to cold welds or hot welds forming within the tip is the other wear mechanism. After a cold or hot weld is formed, the feeder must have sufficient force to shear the weld between the contact tip and wire or failure due to lack of feeding occurs. Like welded joints, the weld may be stronger than the material around it causing the shear to occur in the copper metal or the wire around the weld [20,22].

Prior literature suggests non-copper coated electrodes wear the contact tip inner bore more aggressively. This is due to the greater resistance at the electrical junction and increase in hardness of the outer surface of the wire electrode. The most abrasion occurs at arc ignition, when the electrode is stationary, and there is high current flow required for striking an arc [20]. This higher current flow causes more ohmic heating, increasing the probability of a hot weld forming. When the wire begins feeding after an arc is struck, any hot or cold welds formed will be sheared. Reducing the arc ignition time from 61 ms to 16 ms was found to reduce the abrasion volume by approximately 40 % [20]. Matsui et al. also found that for a given current, wear decreases as wire feed speed increases and suggests that conduction heat transfer is increased due to room temperature wire entering the contact tip.

As the contact tip wears, positional errors occur in the wire electrode as well as potential contaminants such as copper and oxides being transferred to the melt pool [22]. In the case of traditional welding, positioning error can reduce the strength of a welded joint by up to 50 percent [18]. Eventually, a worn contact tip will lead to catastrophic failure in the welding process. This can occur due to the feeder being unable to shear a weld between the electrode and contact tube or from an inability of the contact tip to properly transfer current resulting in an unstable arc and poor metal transfer [18,19]. With respect to WAAM, contact tip wear leads to the breakdown of process monitoring and control schemes. Reference current levels shift, which cause issues in any schemes that rely on this, such as a contact tip to work piece distance control loop.

Quinn et al. developed and proposed an algorithm to define a wear metric from welding signals to detect contact tip wear in process during GMAW [18,19]. They found that the integrand of the power spectral density of voltage in the low frequency regime (0.3 to 4 Hz) increased linearly with contact tip wear and then transitioned to non-linear erratic behavior at extreme wear levels. The low frequency variations in wire feed speed at the contact tip due to wear, leads to variations in the electrode extension and thus arc length which is reflected in the voltage. Failure criteria were defined as the wear metric exceeding a specified threshold or experiencing non-linear behavior [18,19]. Other than this method, the primary method for monitoring contact tips found in standard welding guidelines was developing a time-based maintenance log. With the growth of large-scale wire arc additive manufacturing, components require a high amount of arc time and weld bead length, and the wear of the contact tip should be addressed. Additionally, DED-arc studies often use materials that require uncoated feedstock such as tool steel, maraging steel, and other advanced alloys leading to more aggressive wear conditions than the more common copper coated welding filler wire. This study investigates contact tip wear in the context of DED-arc with a focus on understanding the wear condition of the contact tip with respect to wire fed, the affects of wear on the additive process, and process monitoring schemes to enable an evaluation of the wear state. The contact tip bore area was measured along the bore axis for the first time, in addition to measuring the change in area at the exit. Abrasive wear was observed not only on surface of contact tip, but also on the surface of deposited steel that was transferred to the contact tip. Process signal analysis was performed during the feature engineering step of the machine learning architecture, quantifying impact on key process metrics such as the linear energy density (energy per unit length of weld). This work culminated in development of a machine learning based scheme to provide predictions of the wear state from in process data.

Table 1
Percent composition of ER316LSi wire from OEM.

Element	Fe	Cr	Ni	Mn	Mo	Si	C
ER-316LSi	Bal	18.4	11.5	1.9	2.3	0.79–0.87	0.01

Table 2
Experiment matrix.

Trial	Layers	Arc time (min)	Wire fed (m)
A1	1	3	30.5
A2	1	3	30.5
B1	1	6	62.3
C1	2	12	124.7
D1	3	18	187.0
E1	4	24	249.4
E2[a]	4	24	249.4
F1[a]	5	30	311.7
F2[a]	5	30	343

Note
[a] Indicates trial was stopped due to contact tip failure prior to reaching target wire-fed.

2. Material and methods

2.1. Design of experiments and system configuration

The experiment set was designed to generate a set of contact tips worn to a pre-determined level as measured by the amount of wire fed or arc time, and to generate a sufficient amount of in-situ data for machine learning models. The material chosen was a an uncoated 316LSi stainless steel wire electrode due to wide-spread use across various industries in addition to bare stainless steel wearing the contact tip more aggressively. The wire composition is presented in Table 1 below.

A serpentine toolpath was selected to ensure a high amount of wire fed per layer and to reduce the number of arc ignition events. Experiments consisted of a series of parts with toolpaths measuring from 30 to 300 m of wire fed as shown in the experiment matrix in Table 2. Trials B1-F2 utilized a serpentine toolpath approximately 200 mm by 100 mm in area. While, trial A1 and A2 had smaller toolpath of approximately 100 mm by 100 mm. The spacing between adjacent beads was 8.9 mm in all cases. Experiment A1 and A2 served the purpose of generating contact tips at 30 m of wire fed and the data from these experiments were not used in training models. Trial E2 experienced partial melting of the contact tip during arc extinguishment. Similarly, trials F1 and F2 had a target of 360 m of wire fed (eight layers) but the contact tip experienced failure at approximately 311.7 and 343 m respectively. The in-situ data from F1 and F2 was used in training models; however, the contact tips could not be used for ex-situ characterization.

Table 3
Deposition parameters.

Parameter	
Mode	Pulsed spray
Average voltage (V)	23
Average current (A)	250
Wire feed speed (m/min)	10.4
CTWD (mm)	12.7
Traverse speed (m/min)	0.76
Deposition rate (kg/h)	5.0
Dwell time (s)	180

The welding and motion platform process parameters were held at constant set points during each experimental trial. Deposition process parameters are summarized in Table 3 below. It is worth noting that, the waveform controller was constantly running and adjusting the voltage, current, and wire feed speed during the current and voltage waveform. However, the internal waveform controls do not account for wear in the contact tip.

A retrofit WAAM system consisting of a 3-axis CNC machine and welding power supply was utilized for the depositions. A custom adapter holds the torch to the machine spindle shown in Fig. 1. A PowerWave S500 welder, and 4R220 wire feeder unit were used for the GMAW process. A Windows PC connected to the local machine network facilitated in-situ weld data acquisition with PowerWave Manager.

2.2. Contact tip wear characterization

Following depositions, the contact tips were characterized with scanning electron microscopy, optical profilometry and digital microscopy. Contact tips were sectioned at the center along the longitudinal axis. To allow for repeated sectioning, each contact tip was held in a modified gas diffuser assembly with flat edges.

Each contact tip was scanned using a Keyence VR-6200 optical profilometer which operates using structured light scanning. Each scan consisted of a 7.6 mm by 5.7 mm region of interest yielding an XY lateral resolution of 2.468 μm and height resolution of 4.0 μm. Within the profilometer software, the reference plane was set to a best fit plane containing the areas around the bore. From the topographical scan, the bore area was computed along the length of the contact tip. A simple Python script traversed along the X-direction of each scan extracting Y-Z slices. To compute the area, each Y-Z slice was then numerically integrated with the Trapezoidal Rule, seen in Eq. (1).

$$\int_{0.5}^{2.5} Z(y)dy \approx \sum_{i=1}^{N} \frac{Z(y_{i-1}) + Z(y_i)}{2} \Delta y_i \tag{1}$$

The relative bore area at the exit of the contact tip was computed. A least squares linear regression was implemented to relate the amount of wire fed or sliding distance to the relative bore exit area.

2.3. Arc data aggregation

Following experimental trials, the data from each experiment was aggregated across experimental trials into an aggregate dataset. Prior to the experimental trials, test beads were deposited with the same depositions parameters to determine the pulse waveform frequency which was found to be 230 Hz. For each trial, welder power supply data was collected at 1200 Hz and during aggregation, the arc data (current and voltage) was low pass filtered to 600 Hz with a 10th order Butterworth filter to avoid aliasing. The start and end of each bead were removed due to transient characteristics of the arc ignition and arc extinguishment as well as the associated variation in bead height and thus contact tip to work piece distance [5]. Similarly, data from the corners of the toolpath were removed from the aggregate dataset due to height build up associated with machine deceleration and acceleration [23]. The aggregate dataset is summarized below in Table 4.

Fig. 1. Torch and CNC Spindle.

Table 4
Summary of aggregate dataset.

Wire fed (m)	Time (min)	Data points (10^6)
[0, 62.3]	53	1.9
[62.3, 124.7]	53	1.9
[124.7, 187.0]	44	1.6
[187.0, 249.4]	22	0.8
[249.4, 311.7]	11	0.4
Total	187	6.7

2.4. Machine learning architecture

For both classification and regression, a set of features were generated from the filtered aggregate dataset. A moving window approach was taken with various window sizes to generate the feature space. Standard statistical features such as the four statistical moments (mean, standard deviation, kurtosis and skewness) were computed on the current, voltage, and wire feed speed. In addition, the peak and background current and voltage (from the pulsed waveform) were extracted. The more welding specific features were computed on the pulse waveform based on prior knowledge. The root mean square of the voltage signal in 0 to 10 Hz frequency band was used due to Quinn et al. finding a trend with wear [18]. Similarly, the RMS of the voltage signal about the pulse frequency (200 to 300 Hz) was computed as a feature.

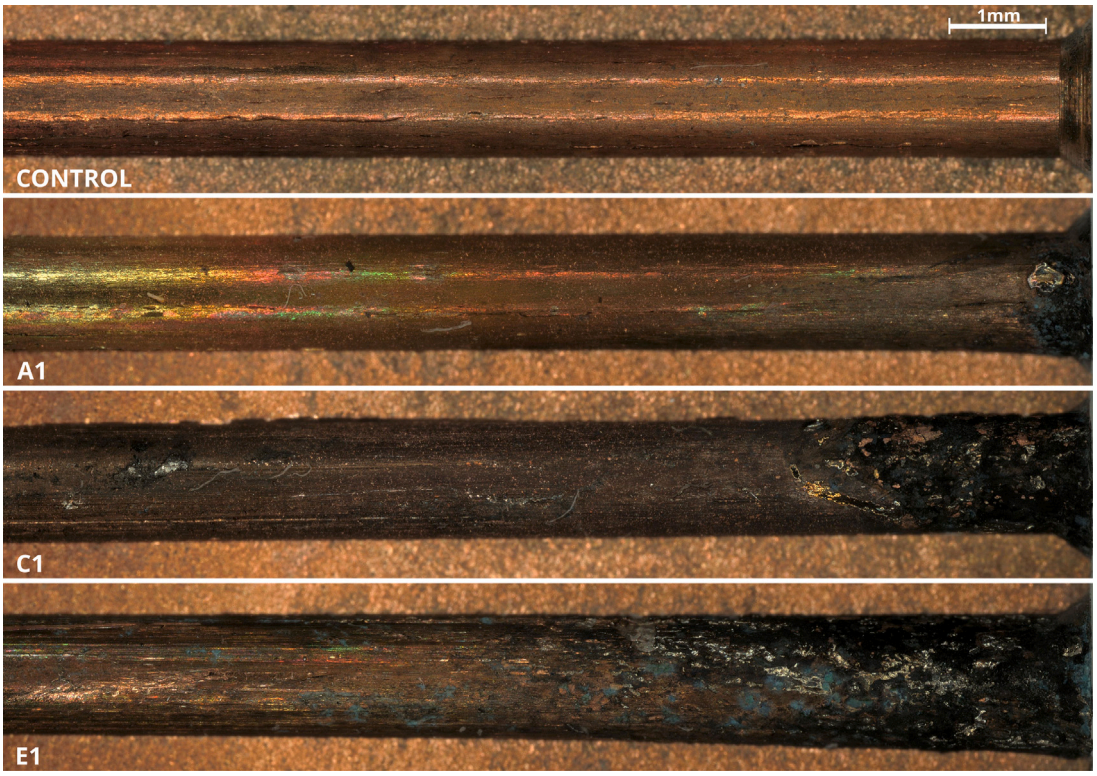

Fig. 2. Digital images of control (factory new), A1, C1, and E1 contact tips.

To capture information about the current and voltage waveform, the time between maximum and minimum extrema of the waveform was measured and statistics on the spectrogram within the frequency band of the pulsed waveform. A complete list of features generated is listed in the appendix along. Formally the feature generation step is described in Eq. (3). The filtered aggregate dataset, composed of the process signal data, is denoted as $3\times N$ matrix, X, where N indicates the total number of data-points collected. The feature matrix is denoted as X', following the feature generation process, X' is $N/M \times 71$ real-valued matrix where M represents the selected windowing size.

$$X \in \mathbb{R}^{3\times N} \rightarrow X' \in \mathbb{R}^{71\times N/M} \tag{2}$$

To perform classification, a random forest was utilized and discrete classes were defined to represent the state of the contact tip at the start of each layer and labeled with the relative bore area from the geometrical analysis regression. These classes corresponded to data collected during the first 15 m of wire fed in each layer as summarized in Table 5. If one were to implement the model live, one would receive an evaluation of the contact tip at the start of each layer and determine whether a replacement is needed. Model hyperparameters were tuned with an exhaustive grid search during which evaluation was performed with a 5-fold cross validation scheme. Evaluation metrics were the f1-score, the harmonic mean of accuracy and precision shown in Eq. (2) [24]. To address the imbalance of the data set due to the nature of the design of experiments, synthetic minority oversampling technique (SMOTE) was implemented after the splitting of the data set for folds, and the train test split. Prior to hyperparameter tuning, the feature space was scaled to have zero mean and unit variance. Once hyperparameters were selected, final model training and evaluation were performed with 75% of the dataset reserved as a training dataset and 25% of dataset reserved as test dataset.

$$f1 = 2\frac{precision * recall}{precision + recall} = \frac{TP}{TP + \frac{1}{2} * (FP + FN)} \tag{3}$$

For regression, a similar approach was taken with a multi-layer perceptron also known as an artificial neural network. No bins were created and the master dataset was continuously labeled with relative bore area. An exhaustive grid search was implemented with coefficient of determination (R^2) function serving as the scoring function, described in Eq. (4)

$$R^2 = 1 - \frac{\sum_{i=1}^{M/N}(y_i - \hat{y}_i)^2}{\sum_{i=1}^{M/N}(y_i - \bar{y})^2} \tag{4}$$

Table 5
Summary of classes.

Label (relative bore area)	Wire fed bin (m)	Data points (10^3)
0.96	[0, 15.2]	460
1.04	[62.3, 77.5]	460
1.14	[124.7, 139.9]	390
1.24	[187.0, 202.2]	190
1.35	[249.4, 264.6]	98

3. Results

The control and worn contact tips were characterized with a variety of methods, including a digital microscope, scanning electron microscope, and optical profilometer. Samples digital images of contact tip A1, C1, and E1 are shown in Fig. 2. Contact Tip A1 had been used for 30 m of wire fed and an arc time of approximately 3 min. The wear region is restricted to around a millimeter from the bore exit, with darkened regions from the welding fumes. A small pad of steel is also visible, this is likely from partial melting of the wire at arc extinguishment. Contact tip C1 was used for 124 m of wire fed (12 min of arc time) and one can observe the increase in length of the wear zone. The area of oxidized surfaces has grown, and there are more dispersed globules of solidified steel present in the wear region. Finally, contact tip E1 was worn with approximately 24 min of arc time and 249 m of wire electrode. By inspection, one can observe not only the increase in length of the wear zone but also the increased width of the bore.

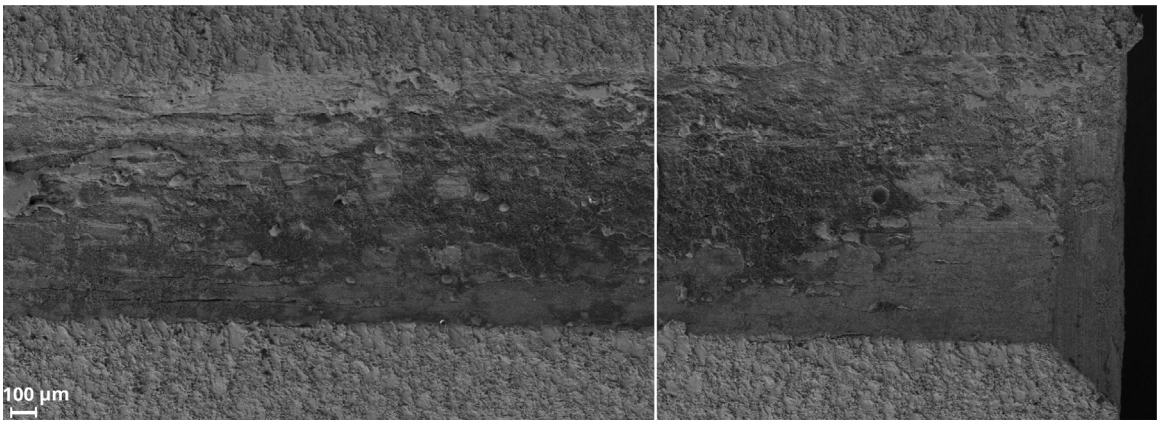

Fig. 3. SEM Images of Bore Exit Region (E1).

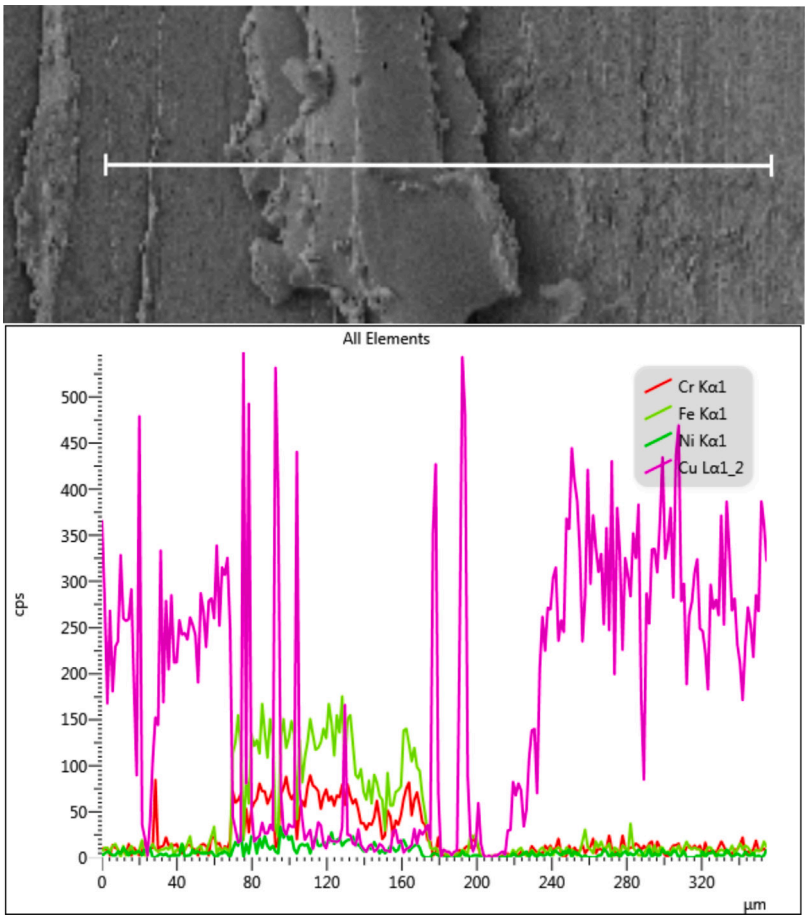

Fig. 4. Line spectrum data from stainless deposit on E1.

3.1. SEM/EDS analysis for material contamination

To confirm potential material contamination within the bore, portions of contact tip E1 were imaged with a scanning electron microscope. Fig. 3 illustrates the exit region of the bore, which has a non-uniform surface, varying in color and texture. One can observe the height difference and damage to the surface in the form of roughness, pock marks, and scratches. Among the oxide surface layer, there are small globules of solidified metal and exposed surfaces.

To confirm the alloy composition and investigate the transition region, a line spectrum was also taken across one of the stainless deposits. Fig. 4 illustrates the spectrum data for the line with counts per second for each metal element of interest (contact tip alloy and 316L alloy elements). In the region containing the deposit, around 70 to 180 µm, there is significantly greater count of iron and chromium with a range of 50 to 150 counts. Additionally, other 316L alloying elements are present at a count less than 50 (Nickel, Molybdenum, Manganese, etc.). Due to these elements' low concentration in 316L, there is less distinction in their counts between the steel deposit region and the bore surface region. An interesting observation is the peaks of copper throughout the 70 to 180 µm range of the steel deposit. This is likely due to the miscibility gap between copper and iron and indicates that melted copper was dispersed in the steel [25]. Liquid phase separation of copper and iron occurs because of the miscibility gap and the copper

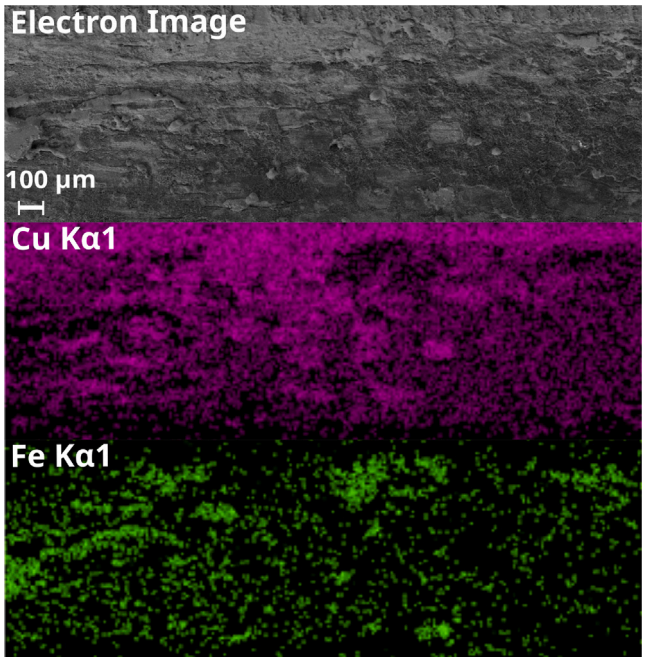

Fig. 5. EDS Map of bore exit region of sample E1.

solidifies first. Subsequently, the steel cools and solidifies. This leads to the formation of copper globules or spherules which matches with the line spectrum data, as the peaks occur at edges or changes in the deposit profile.

Fig. 5 visualizes the energy dispersive spectroscopy map of the bore exit region. This map corroborates later observations made through visual inspection of the digital microscope images. One can also observe that the area of exposed copper surface has been reduced, with some small regions of higher copper concentration remaining. Evidence of small steel deposits are present in the map for iron with iron particles dispersed throughout the region, and small areas of high iron concentration indicating globules of steel.

To confirm abrasive wear, images were taken at 500X (left) and 2000X (right) capturing wear tracks in Fig. 6. The top two images are centered on a portion of the contact tip that had an exposed CuCrZr surface. Parallel scratches are present indicative of abrasion from the steel wire or asperities. Further, the bottom image captured scratches on a previously deposited steel globule. The steel globule likely formed due partial melting at the wire interface with the contact tip or spatter traveling up the tube. Abrasive wear can be inferred from the uniformity in the top-surface as compared to the edges of the globule and other deposited globules. Small beads of copper are embedded in the edges of the globule indicating copper melting and precipitating out of solution as it solidifies.

3.2. Optical profilometry for material loss

From the topographical maps of each contact tip, the area of the bore region was computed with trapezoidal integration as detailed in 2.4. Fig. 7 illustrates the bore area as a function of the position along the bore. The wear region is restricted to the last two millimeters, [10,12] on the X-axis, for the contact tip for A1 and B1. For C1, the wear region has grown to [6, 12] mm and for D1 and E1, the wear region comprises the entire scanned region [0, 12] mm. The geometric results indicate that the wear of D1, and E1 experiences wear further from the exit region. The wear in the [0, 6] millimeter range (further from the exit of the contact tip) is likely only mechanical in nature. This is supported by the lack of solidified steel and carbon further up the bore, observed in digital images.

For comparison to prior literature, and for the machine learning architectures, the area at the exit was extracted from the bore area and position data. The relative exit area for each contact tip is illustrated in Fig. 8. A least squares linear regression was computed, and the line of best fit is shown. The error bars on each area datum represent the total uncertainty from the propagation of uncertainty during numerical integration. The area was found to increase linearly with the amount of wire fed. The maximum increase in area observed was 49 percent in contact C1. The enlargement of the bore will result in a shift in the wire position. By itself, the wire could be mispositioned by up to 0.5 mm at the contact tip exit. However, this position error could reach significant levels at the workpiece when considering sine error over the contact tip to workpiece distance.

3.3. Process signals analysis

To understand how the welding process is affected by the wear of the contact tip, the welding signals were analyzed with the statistical features generated, as well as the linear energy density. Linear energy density is a variable to measure heat input to the weld per unit length. The heat input and wire feed speed to traverse speed ratio are physical measures that affect the resultant weld bead geometry. Additionally, selected features were used to visualize changes to the welding process. Histograms of the selected features were generated from layer 1 and layer 4 data with fixed width bins for each variable. Fig. 9 illustrates the histograms with layer one in blue and layer four in green. The dashed lines in each histogram represent the 95% expectation bounds associated with three standard deviations of the data set. Comparing the histogram of linear energy density, the bounds grow from approximately [430, 480] J/mm to [325, 575] J/mm. Similar observations can be made on the 95% intervals for each feature. In layer 1 the distribution of the WFS standard deviation of has very few instances beyond 2 ipm. By layer 4, there are many datums beyond 2 ipm, which is a signature of poor feeding.

3.4. Machine learning for classification

A random forest classifier (RFC) was utilized to classify the arc data into five distinct classes of wear, as described by the relative change in contact tip area. The feature space and bins for classes are described in Section 2.4. An exhaustive grid search was performed to tune the hyperparameters of the RFC. Two key hyperparameters are the minimum samples split, which described the minimum number of samples to split a node, and the max features, which describes the number of features selected at random when searching for a split. Fig. 10 illustrates the results of a 5-fold cross validated grid search for the minimum samples split and max features hyperparameters, with the color gradient of each cell determined by the mean test score of that hyperparameter combination.

The F1-score described in Eq. (3) was used as the scoring metric. As the minimum number of samples split increases, the performance of the classifier degrades slightly. The best value for minimum samples split was found to be two. Across the domain of max feature hyperparameter, there is not a clear trend between the hyperparameter value and mean test score. However, the range of 12 to 24 gives favorable results at minimum samples split value of two. A value of 16 was chosen for the max features parameter due to the performance and to reduce the risk of overfitting a model.

Following hyperparameter tuning, the random forest classifier was evaluated with 5-fold cross validation at various window sizes. Window size refers to the number of data points used to compute a given feature datum. Increasing the window size increases the amount of time associated for each feature datum, which has an effect of greater smoothing in the time domain as increasing the observation window for wear-related phenomena in the arc data. Decreasing the window size increases the granularity in the data when viewed from the time

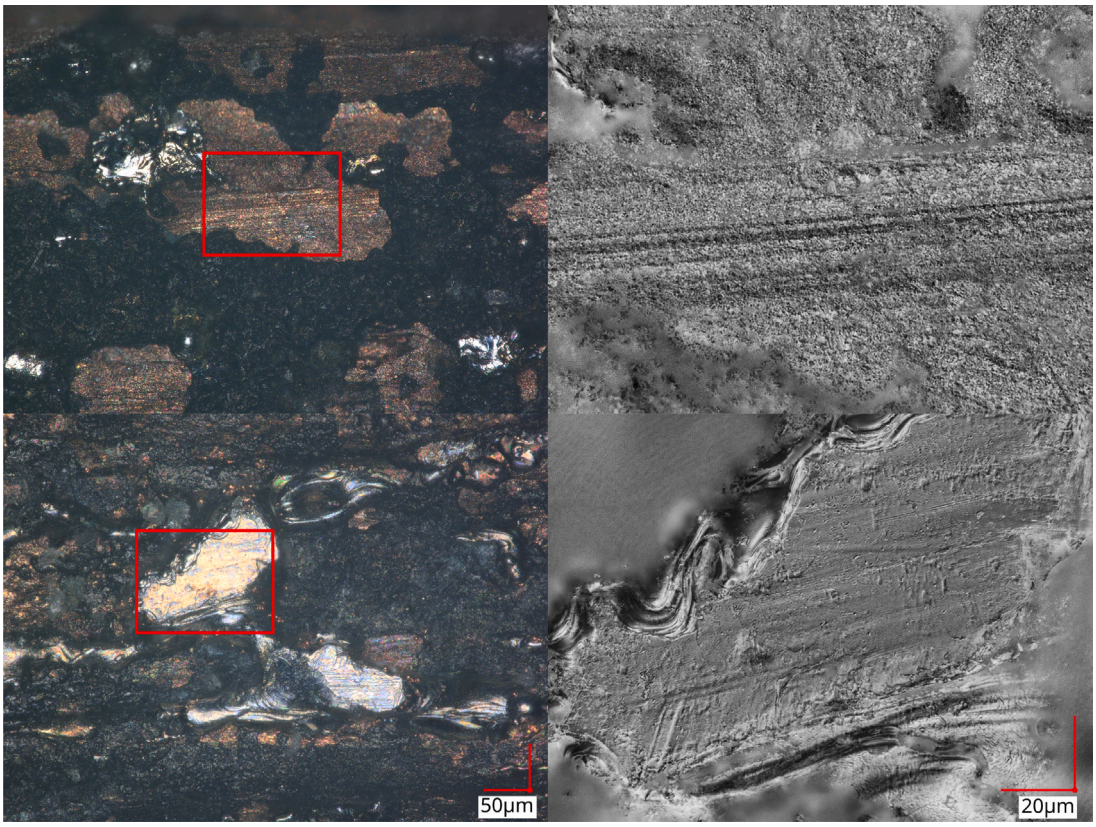

Fig. 6. Wear tracks present on copper and steel surfaces.

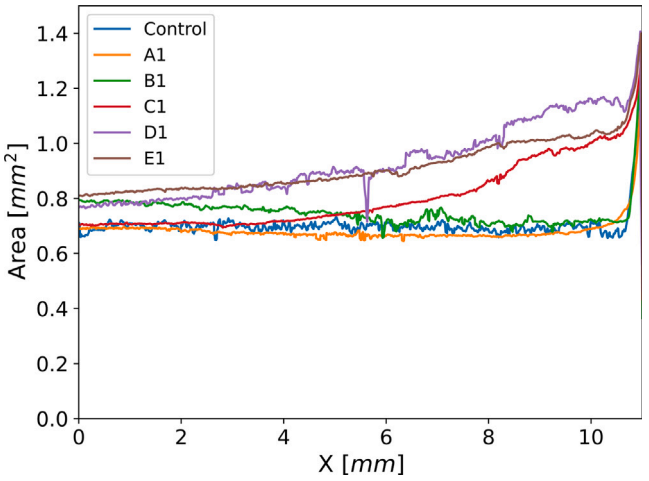

Fig. 7. Bore area as a function of X position along the bore.

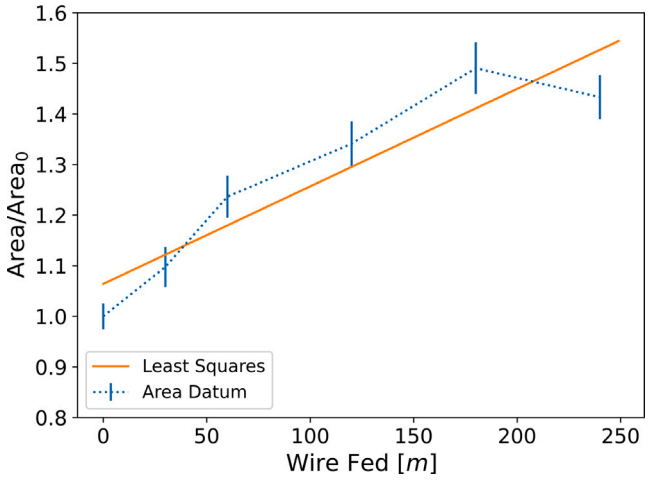

Fig. 8. Relative bore exit area.

domain;however, too small of a window may miss indicators of wear in the arc data and wire feed speed. A summary of the performance of the model for various window sizes is provided in Table 6. The smallest window size of 256 had the lowest F1-score, which is to be expected, as this data will contain a few pulse waveforms where the effects of wear may not be observed. With the window size increased to 512, the F1-score improved to 0.81 ± 0.01. Beyond 1024, model improvements due to smoothing are reduced. The classifier performance exhibited maximum F1-score of 0.84 for window size of 1024. Given this, subsequent machine learning models were evaluated with a window size of 1024 data points. A sample confusion matrix for N = 1024 is shown in Fig. 11

To better understand which features are used by the classification model to make a prediction, the permutation-based feature importance was computed with the trained model. With permutation feature importance, a single feature is corrupted by randomly shuffling the feature column and the associated labels. Fig. 12 illustrated the feature importance as measured by the mean accuracy decrease in the model. For

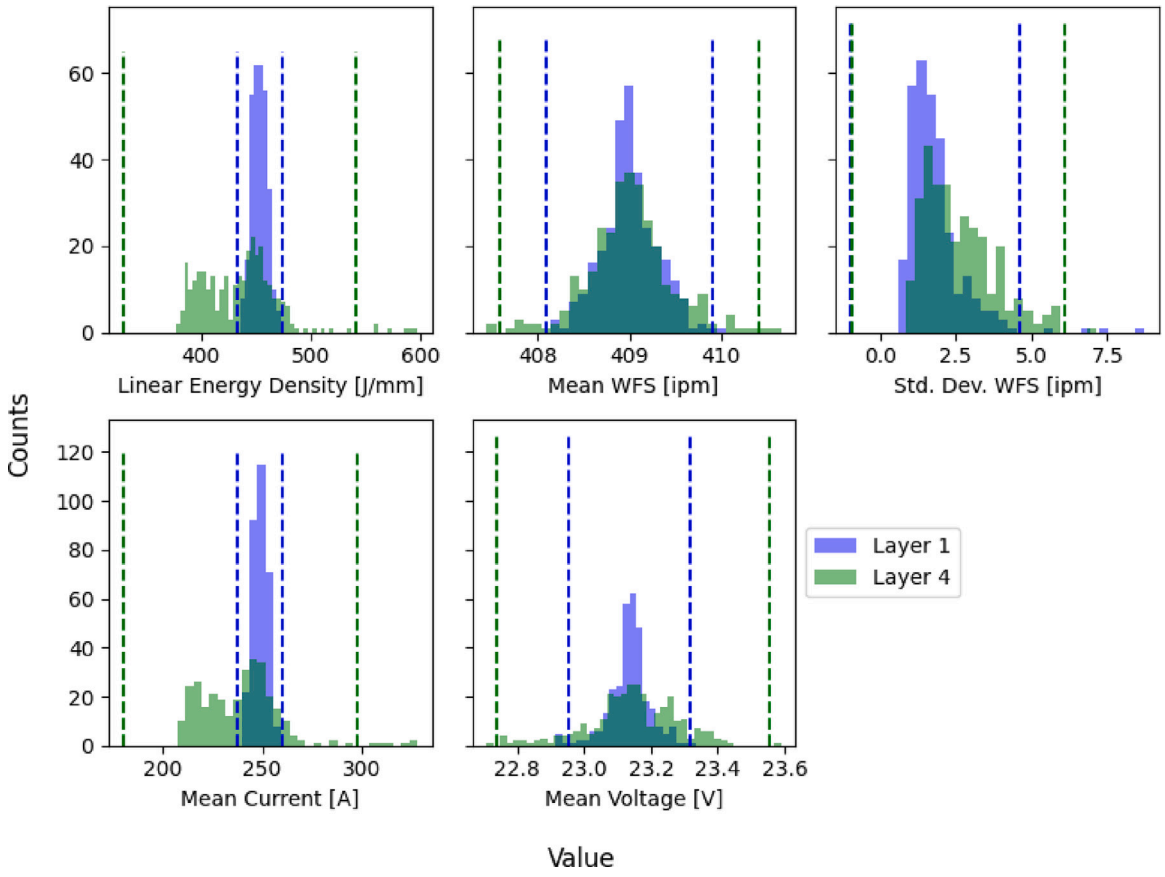

Fig. 9. Histograms of selected features from Trial E1.

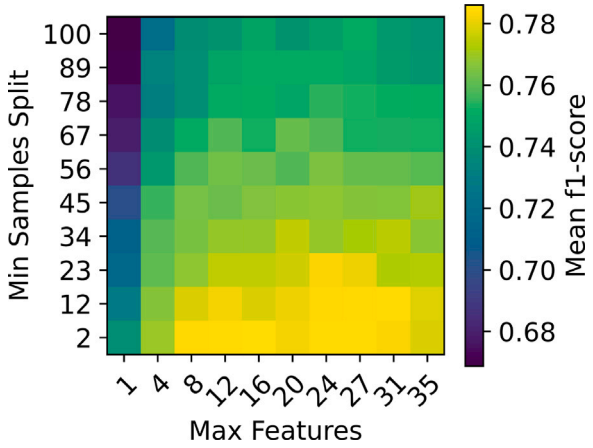

Fig. 10. Hyperparameter tuning with N = 1024.

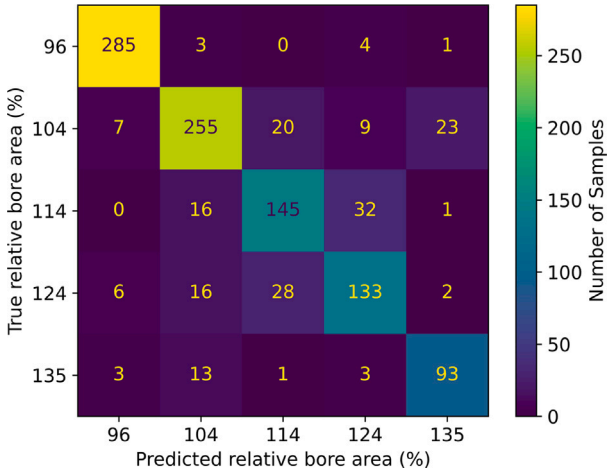

Fig. 11. Confusion matrix visualizing the classification of the data set with a window size of N = 1024.

Table 6
Window size study.

Window size	Window size (ms)	Average f1-score	Standard deviation
256	213	0.79	0.01
512	426	0.81	0.01
1024	853	0.84	0.01
1536	1280	0.82	0.02
2048	1706	0.82	0.03

readability, the top ten features are shown. The permutation corruption of the standard deviation of the voltage reduced the model's accuracy the greatest followed by the standard deviation of the wire feed speed.

3.5. Machine learning for regression

A multilayer perceptron or artificial neural network regressor was developed and evaluated in a similar manner to the classifier. Hyperparameter tuning results from a 5-fold CV grid search are presented in Fig. 13 below. Alpha, or the regularization parameter, was swept from a value of 1E−4 to 1E+3. Potential hidden layer sizes were chosen based on fractional amount of the sum of the input layers (number of features) and output layer (prediction of relative bore area), which is equivalent to 72. As alpha increases from 1E−4, the model performance generally improved across the selection of hidden layers.

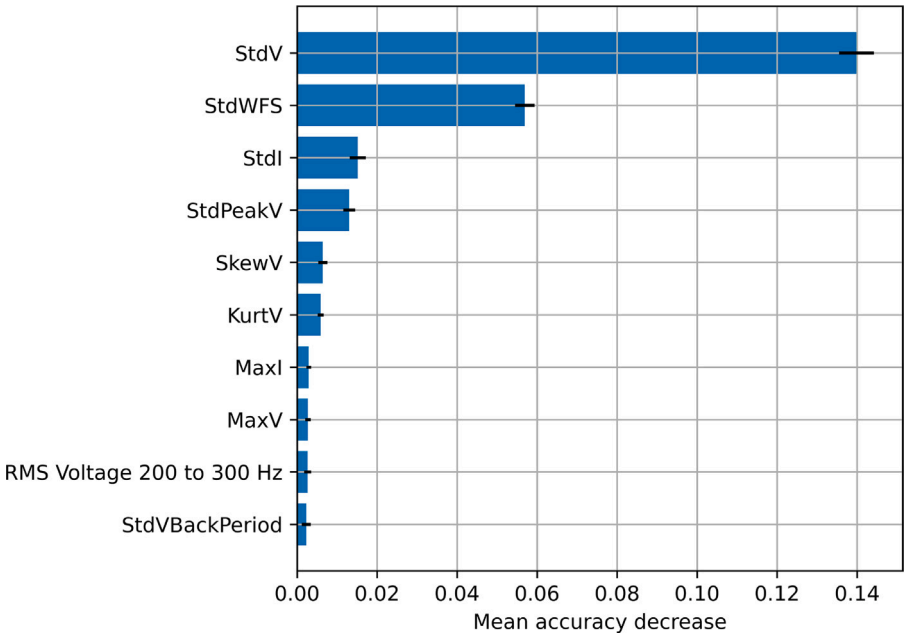

Fig. 12. Permutation feature importance for RFC.

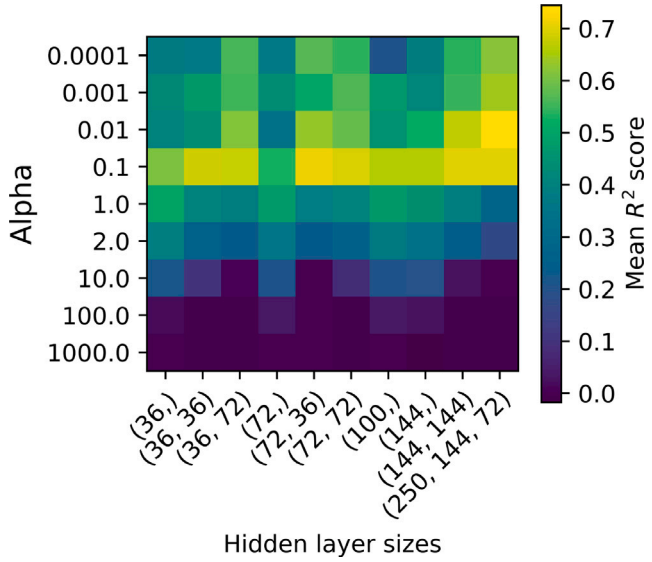

Fig. 13. MLP hyperparameter tuning.

This behavior reverses beyond an alpha of 0.1, with model performance dropping significantly beyond an alpha of 10. The architectures with two hidden layers tended to outperform a single hidden layer, with the best performance achieved with three hidden layers (250, 144, 72). Larger neural network architectures beyond this were avoided to reduce the potential to over-fit the modal.

The MLP regressor was trained and evaluated with an alpha of 0.01, a single output layer, and three hidden layers of 250, 144 and 72 neurons resulting in an R^2 score of 0.75. Fig. 14 provides an overview of the model performance on a 10 percent random sample of the test data set. The MLP regressor tends to shows a favorable balance of over and under-prediction for a significant portion of the predicted domain. This behavior is diminished beyond a value of 1.2 and the model shifts to over-predicting, similar to the transition seen in random forest classifier confusion. This transition is less pronounced with the MLP predicting fewer extreme outliers likely due to the similar predictive features being present across continuous wear values as opposed to discrete bins to classify.

Fig. 15 visualizes the permutation feature importance for the multi-layer perceptron regressor model. Voltage based features dominate the models resultant predictions with the standard deviation of the voltage and the mean background voltage. Physically, the background voltage corresponds to the voltage during the short portion of the waveform, when the electrode and workpiece are shorted through the droplet. Interestingly, permutation of the mean background voltage period or time between shorts, reduced the R^2 score by ≈0.35. Other features of significance for the model include the kurtosis and skew of the voltage signal as well as the mean period of the peaks in the voltage waveform.

4. Discussion

4.1. Model performance

From the process signals to the results of the machine learning models, insights about potential detriments of contact tip wear and the appropriate features to compute for monitoring wear are gained. The random forest classifier shows better performance than the regression model which is likely due to less than thermal biasing of the arc signals and simplifying the problem of predicting wear into classification. With a classification-based approach, an upper limit on the bore wear would be chosen and the model could be implemented as a go/no-go check at the start of each layer. This would provide an evaluation of the current state of the contact tip and allow an operator to quickly determine if it should be changed. The top three important features, as computed with permutation feature importance are the standard deviation of each data stream and the standard deviation of the peak voltage.

The performance of the regression model could likely be improved by further examination of the frequency domain. From the layer 4 histograms of selected features, Fig. 9, one can observe a bimodal distribution indicating that the arc behavior is shifting between stable and unstable behavior when in a worn state. Such alternating behavior may explain why discrete classifiers can sometimes outperform continuous regression models for certain wear states. With the bimodal distribution, some of the feature windows will appear stable and similar in value to layer 1's distribution. Increasing the window size may provide more smoothing at the cost of reducing potential signatures of wear in the arc signal. This effect was observed in the classification model where the performance increased less as the window size increased. From Fig. 15, the most critical feature for this particular model

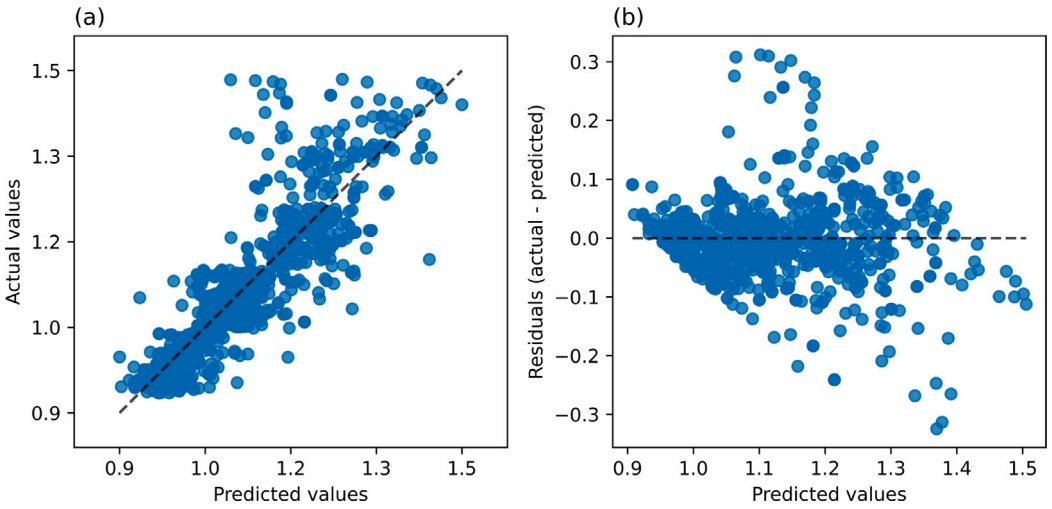

Fig. 14. MLP Performance visualized with a 10% random sample. (a) actual relative bore area against relative bore area (b) residuals compared against predicted values.

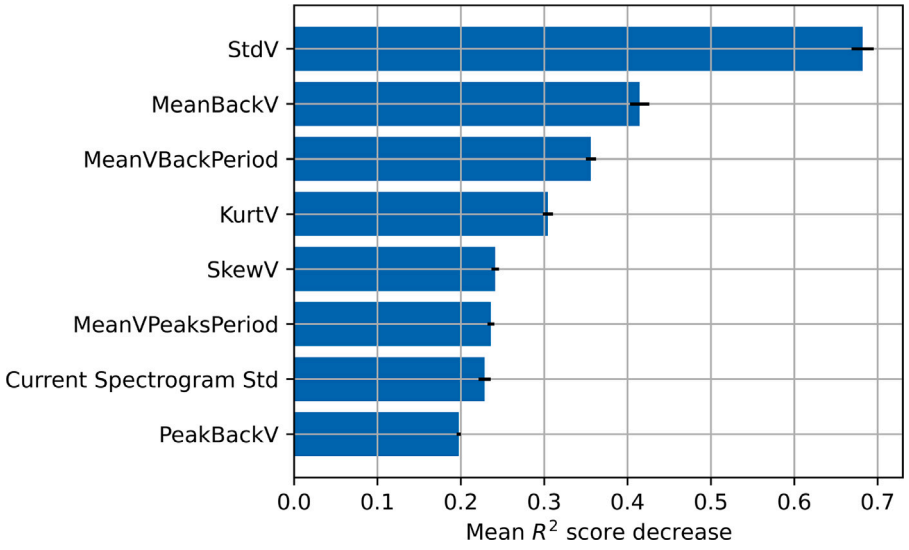

Fig. 15. Permutation based feature importance as measured by the mean R^2 score decrease with the MLP regressor.

is the standard deviation of the voltage, followed by other voltage based features. This is contrasted by the classifier, where standard deviation of the voltage was still the highest ranked feature; however, it was followed by wire feed speed standard deviation, current standard deviation and the standard deviation of the peak voltage. This pattern suggests that classifiers benefit from diverse feature combinations to establish class boundaries, while regression models may rely more heavily on features that vary continuously with wear progression, particularly those related to the short-circuit phase. The MLP regressor appears to better fit data across the domain without overfitting in the portions of the predicted domain. This likely leads to the model performing more reliably than the RFC. Given the characteristics of each model's predictions, the MLP regressor displays a balance of favorable traits with over prediction, a relatively fast training time, and few signs of overfitting. Both models demonstrate some robustness and the ability to make appropriate predictions even if one data stream becomes corrupted, which represents an important consideration when evaluating potential industrial implementations where sensor reliability may vary.

4.2. Contact tip characterization

The physical signs of wear on the contact tip suggest that the variation in voltage is likely due to poor feeding and wire adhesion within the contact tip. The wire feed speed is reported at the roller, while any changes in the wire feed speed at the torch will result in variations in the voltage as the electrical stick out changes. Quinn et al. observed that there is a discrepancy between the wire feed speed at the roller and at the exit of the torch [19]. This is likely why wire feed speed features were less important for the models presented.

SEM and EDS analyses revealed both abrasive and adhesive wear mechanisms operating simultaneously. The observed parallel scratches in Fig. 6 provide evidence of abrasive wear from the steel wire sliding against the copper surface. Meanwhile, the solidified steel globules, especially near the exit region, indicate adhesive wear facilitated by localized heating, aligning with Matsui et al.'s findings [20]. Wear progression patterns suggest a shift in dominant mechanisms over time. In early stages (e.g., contact tip A1 with 30 m of wire fed), mechanical wear dominates and remains localized near the exit. As wire feed increases, thermal effects become more significant, evidenced by increased steel deposits and copper-iron interactions seen in the line spectrum data (Fig. 4). The miscibility gap between copper and iron noted by Curiotto et al. [25] creates conditions where melted copper disperses within steel deposits, potentially creating a cycle of adhesion and abrasion that accelerates wear. The wear closer to the exit region is likely electro-mechanical in nature, with the adhesive/abrasive wear mechanism as described in Section 1. This is supported by indicators of melting and solidification and greater material contamination near

the exit. Additionally, the increase in length of the wear zone indicates that the electrical junction or point of current transfer shifts along the longitudinal axis of the bore. As the bore cross-section becomes enlarged, the point of contact may shift. This would also shift the effective electrical stick out and associated resistance. Overall, the geometrical wear results are similar to prior results in the literature that found a linear relationship between wire feed and material loss or bore enlargement [20,21].

Quinn et al. utilized the PSD of the voltage in the low frequency regime as well as the RMS, which they theorized would capture changes in the electrical stick out due to wear. In this study, the low frequency RMS was found to be less important than the RMS in the pulse frequency for each model's prediction. This may be due to the much higher pulse frequency used in the waveform of the welding power supply as compared to prior studies. Additionally, from the process signal analysis the wear of the contact tip changes both the linear energy density and increases the variation in the wire feed speed. Both of these factors will compound to directly change the weld bead geometry. Linear energy density, a measure of heat input, affects the width and height of the weld bead and the wire feed speed is tied to the mass flow rate or material input into the melt pool [4,26].

The prominence of mean background voltage and mean period of the background voltage (time between shorts) in feature importance suggests specific mechanisms linking contact tip wear to welding process stability. As the bore enlarges, the electrical contact between wire and tip becomes less consistent, potentially creating variations in the short-circuit phase of metal transfer that manifest in the background voltage signal. These variations appear particularly sensitive to wear state, making them valuable diagnostic indicators. The pulsed waveform (230 Hz) likely influences wear progression differently than constant current or constant voltage processes would. Peak current phases may accelerate adhesive wear through increased heating, while background current periods allow cooling and solidification of melted material. This thermal cycling could explain the observed pattern of discrete steel globules rather than continuous deposits. The importance of temporal features like the mean period of voltage peaks supports this interpretation, suggesting that wear affects both the magnitude and timing of metal transfer processes.

5. Conclusion

This research investigated contact tip wear in the context of wire-arc additive manufacturing or DED-arc, providing the first comprehensive characterization of both geometrical wear and material contamination along the entire bore length. This work focuses on a critical consumable component in the welding circuit which should be monitored in large-scale depositions to ensure quality outcomes. A novel framework was developed to assess the wear state of the contact tip utilizing in-process arc data collected from a welding power supply during the DED-arc process, eliminating the need for additional sensors or process interruption. Evidence of abrasive and adhesive wear mechanisms were found in this study, with the first documented observation of wear tracks present in both the copper surface and steel globules that were deposited in the bore. Material contamination due to adhesive wear and spatter travel were characterized with EDS, revealing a complex interaction between the copper contact tip material and steel deposits, including evidence of liquid phase separation during solidification.

Statistical changes in key process indicators such as linear energy density, wire feed speed, and the current and voltage demonstrated the impact of wear on process stability. A random forest classifier achieved a cross-validated f1-score of 0.84 for discrete wear states, while a multi-layer perceptron regressor demonstrated an R^2 score of 0.75 for continuous prediction of bore enlargement. These models could be deployed in industrial settings through integration with existing welding power supplies, providing real-time evaluation of contact tip condition at the start of each layer. Such capability would enable automated maintenance scheduling and prevent quality issues before in the deposited material. For manufacturers, this translates to reduced material waste, improved process reliability, and better documentation of consumable life cycles.

Most significantly, this work establishes a foundation for transforming contact tip wear from an unpredictable failure mode into a monitored and managed process variable. By leveraging readily available electrical signals through appropriate feature extraction and machine learning techniques, depositions systems can implement real-time monitoring without additional sensors or equipment. Future development of this approach should focus on validating the models across broader material combinations and process parameters, with particular emphasis on integrating wear monitoring into closed-loop control systems to compensate for the affect of wear on arc signals.

CRediT authorship contribution statement

Zaky Hussein: Writing – original draft, Visualization, Validation, Software, Methodology, Investigation, Conceptualization. **Katherine Fu:** Writing – review & editing, Supervision, Methodology, Funding acquisition, Conceptualization. **Kyle Saleeby:** Project administration, Supervision, Writing – review & editing. **Christopher Saldaña:** Writing – review & editing, Supervision, Project administration, Methodology, Funding acquisition, Conceptualization.

Declaration of competing interest

The authors declare that they have no known competing financial interests or personal relationships that could have appeared to influence the work reported in this paper.

Acknowledgments

Funding for this work was supported through Department of Energy award number DE-EE0008303. The authors would like to acknowledge the staff of Georgia Tech Advanced Manufacturing Pilot Facility and A. Burl for their guidance and feedback.

Appendix. List of features

A full list of features are listed in Tables A.7–A.9.

Table A.7
Current-based features.

Current features
Mean current
Maximum current
Minimum current
Maximum minus minimum current
Mean sum of squares
Counts of values above mean
Standard deviation
Kurtosis current
Skewness current
Mean peak current
Standard deviation peak current
Kurtosis peak current
Skewness peak current
Mean background current
Standard deviation background current
Kurtosis background current
Skewness background current
Mean peak minus mean background current

Table A.8
Voltage-based features.

Voltage features
Mean voltage
Maximum voltage
Minimum voltage
Maximum minus minimum voltage
Mean sum of squares
Counts of values above mean
Standard deviation
Kurtosis voltage
Skewness voltage
Mean peak voltage
Standard deviation peak voltage
Kurtosis peak voltage
Skewness peak voltage
Mean background voltage
Standard deviation background voltage
Kurtosis background voltage
Skewness background voltage
Mean peak minus mean background voltage

Table A.9
Additional features.

Additional features
Mean wire feed speed
Standard deviation wire feed speed
Kurtosis wire feed speed
Skewness wire feed speed
Mean resistance
Mean peak resistance
Mean background Resistance
Mean peak minus mean background resistance

References

[1] Karunakaran KP, Suryakumar S, Pushpa V, Akula S. Low cost integration of additive and subtractive processes for hybrid layered manufacturing. Robot Comput-Integr Manuf 2010;26(5):490–9. http://dx.doi.org/10.1016/j.rcim.2010.03.008, Publisher: Elsevier.

[2] Greer C, Nycz A, Noakes M, Richardson B, Post B, Kurfess T, Love L. Introduction to the design rules for Metal Big Area Additive Manufacturing. Addit Manuf 2019;27(November 2018):159–66. http://dx.doi.org/10.1016/j.addma.2019.02.016, Publisher: Elsevier.

[3] Xia C, Pan Z, Polden J, Li H, Xu Y, Chen S, Zhang Y. A review on wire arc additive manufacturing: Monitoring, control and a framework of automated system. J Manuf Syst 2020;57(July):31–45. http://dx.doi.org/10.1016/j.jmsy.2020.08.008, Publisher: Elsevier.

[4] Rodrigues TA, Duarte V, Miranda RM, Santos TG, Oliveira JP. Current status and perspectives on wire and arc additive manufacturing (WAAM). Materials 2019;12(7). http://dx.doi.org/10.3390/ma12071121.

[5] Pattanayak S, Sahoo SK. Gas metal arc welding based additive manufacturing—a review. CIRP J Manuf Sci Technol 2021;33:398–442. http://dx.doi.org/10.1016/j.cirpj.2021.04.010, URL https://www.sciencedirect.com/science/article/pii/S1755581721000675.

[6] Venturini G, Montevecchi F, Scippa A, Campatelli G. Optimization of WAAM deposition patterns for T-crossing features. Procedia CIRP 2016;55:95–100. http://dx.doi.org/10.1016/j.procir.2016.08.043, Publisher: The Author(s).

[7] Wu B, Pan Z, Ding D, Cuiuri D, Li H, Xu J, Norrish J. A review of the wire arc additive manufacturing of metals: properties, defects and quality improvement. J Manuf Process 2018;35(February):127–39. http://dx.doi.org/10.1016/j.jmapro.2018.08.001, Publisher: Elsevier.

[8] Xiong J, Zhang G, Hu J, Wu L. Bead geometry prediction for robotic GMAW-based rapid manufacturing through a neural network and a second-order regression analysis. J Intell Manuf 2014;25(1):157–63. http://dx.doi.org/10.1007/s10845-012-0682-1.

[9] Jin C, Shin S, Yu J, Rhee S. Prediction model for back-bead monitoring during gas metal arc welding using supervised deep learning. IEEE Access 2020;8:224044–58. http://dx.doi.org/10.1109/ACCESS.2020.3041274.

[10] Li Y, Polden J, Pan Z, Cui J, Xia C, He F, Mu H, Li H, Wang L. A defect detection system for wire arc additive manufacturing using incremental learning. J Ind Inf Integr 2022;27:100291. http://dx.doi.org/10.1016/j.jii.2021.100291, URL https://linkinghub.elsevier.com/retrieve/pii/S2452414X21000881.

[11] Wei E, Farson D, Richardson R, Ludewig H. Detection of weld surface porosity by statistical analysis of arc current in gas metal arc welding. J Manuf Process 2001;3(1):50–9. http://dx.doi.org/10.1016/S1526-6125(01)70033-3, URL https://www.sciencedirect.com/science/article/pii/S1526612501700333.

[12] Zhang Z, Chen X, Chen H, Zhong J, Chen S. Online welding quality monitoring based on feature extraction of arc voltage signal. Int J Adv Manuf Technol 2014;70(9):1661–71. http://dx.doi.org/10.1007/s00170-013-5402-2.

[13] Horn M, Schmitt M, Langer L, Schlick G, Seidel C. Laser powder bed fusion recoater selection guide—Comparison of resulting powder bed properties and part quality. Powder Technol 2024;434:119356. http://dx.doi.org/10.1016/j.powtec.2023.119356, URL https://linkinghub.elsevier.com/retrieve/pii/S0032591023011403.

[14] Massey CE, Saldaña CJ. On the nature of recoater damage powder spreading mechanics. 2024, http://dx.doi.org/10.26153/TSW/58217, URL https://repositories.lib.utexas.edu/handle/2152/130869, Publisher: University of Texas at Austin.

[15] Liu J-R, Chiang P-J. Novel real-time structured light 3D scanning technique for powder bed state and recoater wear analysis in powder bed fusion. Measurement 2025;239:115463. http://dx.doi.org/10.1016/j.measurement.2024.115463, URL https://linkinghub.elsevier.com/retrieve/pii/S0263224124013484.

[16] Yang J, Ji S, Eo D-R, Yoon J, Kahhal P, Lee H, Park S-H. Effect of abnormal powder feeding on mechanical properties of fabricated part in directed energy deposition. Int J Precis Eng Manuf- Green Technol 2024;11(6):1781–96. http://dx.doi.org/10.1007/s40684-024-00620-0, URL https://link.springer.com/10.1007/s40684-024-00620-0.

[17] DeWitte L, Saldana C, Kurfess T, Fu K. Effect of coaxial nozzle wear on catchment efficiency in direct energy deposition built components. J Manuf Syst 2022;63:524–38. http://dx.doi.org/10.1016/j.jmsy.2022.05.004, URL https://linkinghub.elsevier.com/retrieve/pii/S0278612522000747.

[18] Quinn TP, Madigan RB, Mornis MA, Siewert TA. Contact tube wear detection in gas metal arc welding. Weld J (Miami, Fla) 1995;74(4):115–21.

[19] Mornis MA, Quinn TP, Siewart TA, Steele JPH. Sensing of contact tube wear in gas metal arc welding. U. S Dep Commerece, Natl Inst Stand Technol 1992.

[20] Matsui H, Hattori T. Abrasion phenomena of the contact tip in consumable electrode arc welding. Weld Int 2018;32(7):475–84. http://dx.doi.org/10.1080/01431161.2017.1346886, Publisher: Taylor & Francis.

[21] López LA, Perez GY, Garcia FJ, López VH. Study of GMAW process parameters on the mechanisms of wear in contact tips C12200 alloy. MRS Online Proc Libr 2015;1766(1):53–62. http://dx.doi.org/10.1557/opl.2015.412.

[22] Shimizu H, Yokota Y, Mizuno M, Kurokawa T. Wear mechanism in contact tube. Sci Technol Weld Join 2006;11(1):94–105. http://dx.doi.org/10.1179/174329306X77885, URL http://journals.sagepub.com/doi/10.1179/174329306X77885.

[23] Li F, Chen S, Wu Z, Yan Z. Adaptive process control of wire and arc additive manufacturing for fabricating complex-shaped components. Int J Adv Manuf Technol 2018;96(1–4):871–9. http://dx.doi.org/10.1007/s00170-018-1590-0, Publisher: The International Journal of Advanced Manufacturing Technology.

[24] Berry MW, Mohamed A, Yap BW, editors. Supervised and unsupervised learning for data science. Unsupervised and semi-supervised learning, Cham: Springer International Publishing; 2020, http://dx.doi.org/10.1007/978-3-030-22475-2, URL http://link.springer.com/10.1007/978-3-030-22475-2.

[25] Curiotto S, Greco R, Pryds N, Johnson E, Battezzati L. The liquid metastable miscibility gap in Cu-based systems. Fluid Phase Equilib 2007;256(1–2):132–6. http://dx.doi.org/10.1016/j.fluid.2006.10.003, URL https://linkinghub.elsevier.com/retrieve/pii/S0378381206004316.

[26] Thien A, Goodwin J, Saldana C. Effects of process parameters on thin-wall substrate WAAM deposition. In: Volume 2: manufacturing processes; manufacturing systems. West Lafayette, Indiana, USA: American Society of Mechanical Engineers; 2022, V002T05A004. http://dx.doi.org/10.1115/MSEC2022-80707, URL https://asmedigitalcollection.asme.org/MSEC/proceedings/MSEC2022/85819/V002T05A004/1147009.